A. De Gaspari, V. Cavalieri, N. Fonzi, S. Ricci
Final Validation and Performance Assessment of a Full-Scale Morphing Droop Nose Demonstrator
in: AIAA Scitech 2023 Forum, AIAA, 2023, ISBN: 9781624106996, p. 1-13, AIAA 2023-2235
[AIAA Scitech 2023 Forum, National Harbor, MD, USA & Online, 23-27 Jan. 2023]
doi:10.2514/6.2023-2235

ACKNOWLEDGEMENTS
The project leading to this application has received funding from the Clean Sky 2 Joint Undertaking (JU) under grant agreement No 807089. The JU receives support from the European Union's Horizon 2020 research and innovation programme and the Clean Sky 2 JU members other than the Union.

Final validation and performance assessment of a full–scale morphing droop nose demonstrator

Alessandro De Gaspari*, Vittorio Cavalieri†, Nicola Fonzi‡ and Sergio Ricci§
Politecnico di Milano, Department of Aerospace Science and Technology, 20156 Milano, Italy

Morphing wing devices based on the active camber concept can improve the aircraft performances in take-off and landing maneuvers. In this paper, a multi-level optimization procedure has been applied to the design of a morphing Droop Nose, in the framework of Clean Sky 2 REG-IADP AIRGREEN 2 project. The adopted procedure deals with the multi-disciplinary aspects of the design, testing, and validation phases. Starting from the initial requirements, the design of a full-scale prototype has been achieved, followed by the manufacturing and the experimental testing to assess the effectiveness of the proposed morphing technology. The experimental results have been used to evaluate the quality of the deformed shape. Moreover, numerical–experimental correlation has been performed to obtain an updated numerical model able to reproduce the behavior of the manufactured demonstrator. Finally, the aerodynamic analysis of the morphing droop nose completes the performance assessment.

I. Introduction

In the field of morphing wings, the active camber concept can be used to design high–lift devices able to improve the aerodynamic performances in take-off and landing maneuvers. Several concepts of variable–camber wings have been proposed over the years, beginning at NASA and Boeing [1–4]. Recently, Flexsys Inc. [5] worked on seamless hinge–free wings able to adapt leading–edge and trailing–edge surfaces to different flight conditions. A flight tests campaign has also demonstrated how fully–compliant morphing devices can replace an entire flap on the NASA Gulfstream aircraft. Different projects have been also funded by the European Union, involving many Universities and research centers in the design of active camber leading–edge and trailing–edge devices [6–8].

The so–called morphing paradox is the most important requirement in the design of morphing devices. On the one hand morphing structures should be as flexible as possible to enable the shape change that ensures the achievement of the required aerodynamic performance with the least actuation energy demand. On the other hand they should be rigid enough not only to withstand the external loads, but to be insensitive to any variation of external loads. This aspect appears clear thinking about the behavior of any control surface. A position command sent to the morphing device must necessarily produce the same shape variation whatever the external load applied. The same shape quality requirement must be fulfilled without the external aerodynamic loads when, for example, the device is actuated in laboratory during a ground test, as well as with the aerodynamic pressure applied to the skin during wind tunnel or flight tests. This requirement is often in conflict with manufacturing and technological aspects related to the development of devices that can be installed on real aircraft. From this point of view it is important that the morphing device is fully flexible, without mechanical hinges that transmit forces from the mechanism to the skin. Any rigid part or mechanical organ could affect the deformed shape, preventing the device from reaching the optimal aerodynamic shape once it is actuated [9]. Compliant structures represent an interesting solution that spreads the elastic deformation inside the entire structure, reducing stress concentrations and helping to achieve the required shape.

For all these reasons, the design of morphing devices is a challenging task that must be addressed with tools able to catch the strong coupling that characterizes compliant structures [10]. Dedicated design procedures, based on optimization techniques, should be adopted. Moreover, experimental testing at full–scale level assumes a key role inside the design process to verify that the difference in behavior between loaded and unloaded condition is negligible.

In the last 15 years the Department of Aerospace Science and Technology at Politecnico di Milano (Polimi) has acquired experience on the design of morphing devices participating in several research projects. A complete multi–level design procedure has been developed, based on optimization tools, to deal with the multi–disciplinary aspects of the

*Assistant Professor, Politecnico di Milano, Department of Aerospace Science and Technology, via La Masa 34, 20156 Milano, Italy
†Ph.D. Fellow, Politecnico di Milano, Department of Aerospace Science and Technology, via La Masa 34, 20156 Milano, Italy
‡Ph.D. Candidate, Politecnico di Milano, Department of Aerospace Science and Technology, via La Masa 34, 20156 Milano, Italy
§Full Professor, Politecnico di Milano, Department of Aerospace Science and Technology, via La Masa 34, 20156 Milano, Italy

design [11, 12]. The procedure aims at the design of a fully compliant structure able, once actuated, to match an optimal shape able to guarantee the aerodynamic performance requirements. The procedure has been applied to the design of a morphing droop nose, in the framework of Clean Sky 2 REG-IADP AIRGREEN 2 project. The multi–level procedure, depicted in Fig. 1, consists of design steps, followed by validation steps. The design phase is composed by three main steps: an aero–structural shape optimization to define the optimal morphing shape able to satisfy the performance requirements; a structural topology optimization to synthesize a compliant structure able to deform itself to match the optimal shape obtained in the previous step; a structural sizing and shape optimization to refine the solution, increasing the fidelity of the result. The adopted tools can be also applied to deal with design modifications or to realize experimental demonstrators. After the design phase, the validation phase is composed of three steps conceived to assess the designed device: assessment of the virtual demonstrator in terms of structural feasibility, 3D shape quality, interaction with wing–box, bird–strike resistance; experimental testing to assess the functionality of a ground demonstrator; aerodynamic and aeroelastic validation of the device performances.

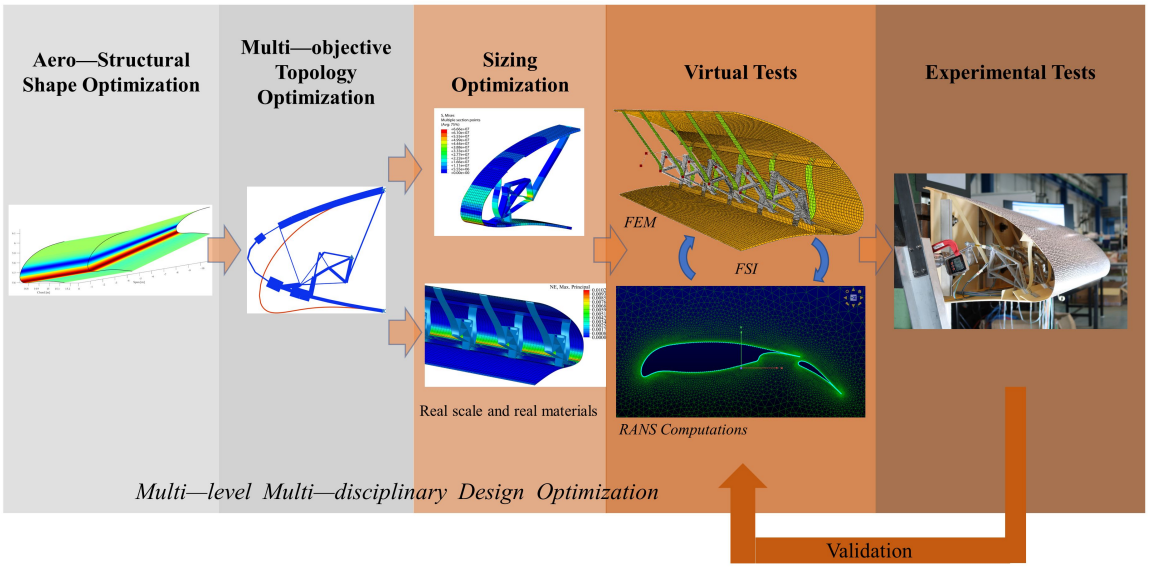

Fig. 1 Multi–level multi–disciplinary optimization procedure for the design and validation of the morphing droop nose.

After summarizing the design procedure of the device, this paper describes the experimental testing of a full–scale prototype to assess the functionality and to evaluate the shape quality. Then, starting from the experimental measures, the higher–fidelity model is updated and the aerodynamic verification is used to validate the performances of the device. The main concern of the work is to assess that the structural design of the device can guarantee a morphing shape change able to provide the required aerodynamic performances. In particular, the aerodynamic analysis of the deformed shape of the morphing prototype will be compared with the analysis of the target shape to assess the difference between the actual solution and the optimal target one, and also to verify that the aerodynamic performances are not compromised by the structural compliance of the device.

II. Design Procedure

The methodological procedure adopted in this work reflects the multi–level approach shown in Fig. 1 and includes the design steps applied to the development of a morphing droop nose that can be installed on the regional aircraft of Clean Sky 2 REG-IADP project. The morphing droop nose is a device conceived to delay the wing stall in high–lift conditions. At the same time the device must preserve the Natural Laminar Flow (NLF) wing shape in cruise, and this is possible thanks to the continuity of the skin. An internal compliant structure, connected to a rotary electromechanical

actuator through a kinematic chain, must be designed to deform the flexible skin to produce an external shape change able to guarantee the design requirements in terms of aerodynamic performances. The aerodynamic requirements for the morphing droop nose prescribe a minimum increment of the aircraft lift coefficient: 2.5% in take-off and 1.8% in landing configuration.

The design of the compliant structure starts from the definition of the optimal morphing shape able to guarantee the performance requirements. Then, an internal structure, able to achieve the optimal target shape is synthesized. At the beginning, a Class/Shape function Transformation (CST) parametric technique [13], extended to work with 3D morphing shapes, is used to describe the wing geometry by using few design variables. The parametric representation is able to introduce the shape changes related to the design variables. Moreover, it is also possible to compute useful information on the structural behavior, such as the bending strains inside the skin when its shape changes. Thanks to this approach, an aerodynamic shape optimization with structural constraints is adopted (first design step). The objective of the optimization is to maximize the droop nose deflection, whereas the constraints assure the structural feasibility of the solution. The aerodynamic simulations are performed by Reynolds Averaged Navier–Stokes (RANS) computations. The optimal morphing shape found by the optimization procedure is represented in Fig. 2. It is able to satisfy the design requirements: the increase of the stall angle is 2.5 deg in the take-off configuration, whereas it is 5 deg in landing configuration [14]. The maximum lift coefficients in the two conditions are higher than the design requirements.

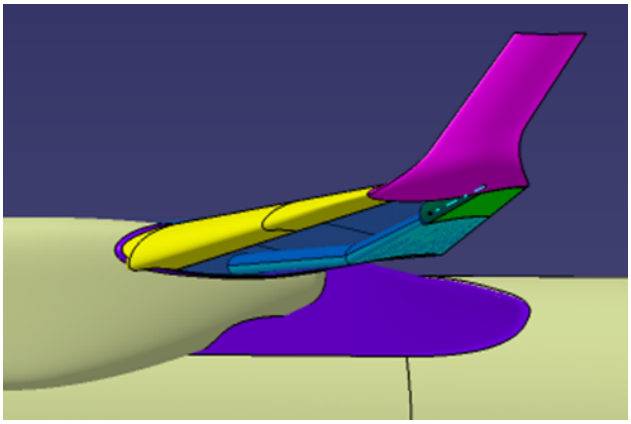

Fig. 2 Optimal target shape of the morphing droop nose for the advanced regional aircraft.

The defined optimal shape represents the target that must be achieved by the compliant structure when actuated. The synthesis of the compliant structure is conducted by using a topology optimization based on a Load Path Representation. A dedicated multi–objective genetic algorithm is used to find the optimal trade–off between the kinematic and structural conflicting requirements (second design step). In particular, the minimization of the Least Square Error (LSE) between the target shape and the skin deformed shape aims at realizing a compliant structure able to perform a shape change matching the target morphing configuration. Moreover, the minimization of the Strain Energy of the structure aims at preserving the NLF wing shape in the undeformed configuration. The multi–objective approach of the genetic algorithm finds several optimal solutions, defining a Pareto Front. Among the available solutions, the designer takes care of selecting a suitable topology solution considering requirements not included in the optimization procedure, such as avoiding excessive difficulties in the manufacturing process. The described optimization computes its objectives based on nonlinear analyses, performed on low–fidelity finite element models (FEM). The selected solution represents the starting point to perform further optimization analyses for the refinement of the solution, based on medium–fidelity FEM models (third design step). In particular, a sizing optimization acting on the thickness distribution of the compliant structure is used to locally refine the global solution of the previous step, trying to improve the kinematic requirement, while not violating the structural one nor the structural feasibility. The described optimization tools are adopted to design the compliant structure of the morphing droop nose, which is represented in Fig. 3.

The complete full-scale device attached to the wing-box is shown in Fig. 4a. After the design and the numerical assessment of the complete device, a demonstrator has been conceived to experimentally validate the proposed concept at the full-scale level. The experimental prototype is depicted in Fig. 4b. It is characterized by the same scale of the complete device, but has a lower span, equal to 1.3 m.

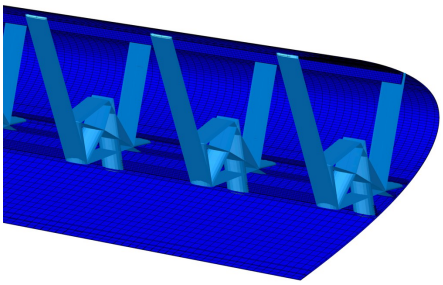

Fig. 3 Topological solution for the internal structure of the morphing droop nose.

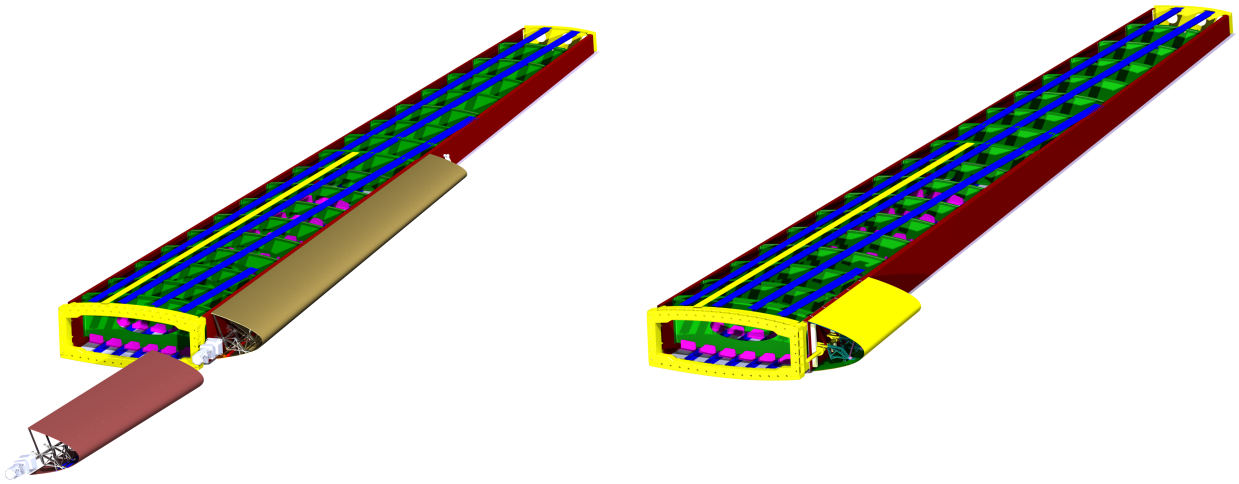

(a) **(b)**

Fig. 4 Morphing droop nose installed on the wing-box: complete device (a) and experimental demonstrator (b).

III. Experimental Prototype

The optimization tools described in the previous section are adopted to finalize the design of the morphing droop nose demonstrator, up to the realization of a full–scale virtual prototype of the device. The full–scale ground demonstrator is designed based on the use of aeronautical materials, namely aluminium alloy and glass–fibre composite material. The prototype shares the same topology solution selected in the design procedure. The design of this model is based on a sizing optimization trying to minimize the error between the deformed and the target shape, while limiting the strain in the compliant structure. The sizing variables of the optimization are the in-plane thickness of each path of the rib and the thickness of ten skin sectors in which the skin is divided along the arc-length of the airfoil. The finite element model used in the optimization loop consists of a single rib placed at the centre of a skin sector, whose span is equal to the rib spacing of 260 mm. The model is made of shell elements for the skin and beam elements for the rib.

After the definition of the optimal sizing variables, a detailed high-fidelity FEM model of the prototype is realized, as shown in Fig. 5. This model is used to validate the solution in terms of structural feasibility and quality of the 3D morphing shape. The model consists of five equally spaced ribs, the skin, and four stringers in correspondence of the connection between ribs and skin. The span of the device is 1.3 m. The wing geometry is slightly tapered, so that the ratio between the tip chord and the root chord of the leading-edge device is 0.94. The rib sections are perpendicular to the spar. The width of each rib is 40 mm and the rib spacing is 260 mm. Regarding the finite element modelling, solid elements are used for the the ribs, whereas skin and stringers are modelled with shell elements. The connection of the ribs to the skin takes place in correspondence of the stringers. Tied constraints are used for these connections, and also to connect the shell elements of the ribs longest paths to the stringers and to the central body of the ribs. The actuation mechanism conceived to achieve the morphing shape change is a kinematic chain made of shaft, cams and rods. It is modelled using rigid elements connected by hinges. Concerning the selection of the materials, the S glass-fibre fabric is

used for the skin, the stringers, and the longest paths of the ribs. The material chosen for the central body of the ribs is the high resistance 7075 aluminium alloy. The estimated mass per unit length of the compliant structure (ribs and skin) is 9 kg/m.

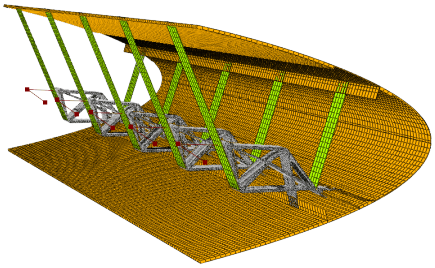

Fig. 5 High–fidelity FEM model of the full–scale prototype.

Nonlinear FEM analyses are performed with the imposition of the shaft rotation to simulate the behavior of the device when actuated. The FEM results of the virtual demonstrator show that the 3D morphing deformation without external load applied is in good agreement with the target shape, as depicted in Fig. 6a. This shape corresponds to a 80 deg rotation of the shaft. Regarding the structural assessment, Tsai-Hill criterion is used to verify each part made in composite material. The failure index in the skin is reported in Fig. 6b. Its maximum value is 0.79. Maximum Von Mises stress in the aluminium ribs is not critical. When the aerodynamic pressure loads are applied to the external surface of the device, there is a slight change in the comparison between deformed and target shapes, as shown in Fig. 6a.

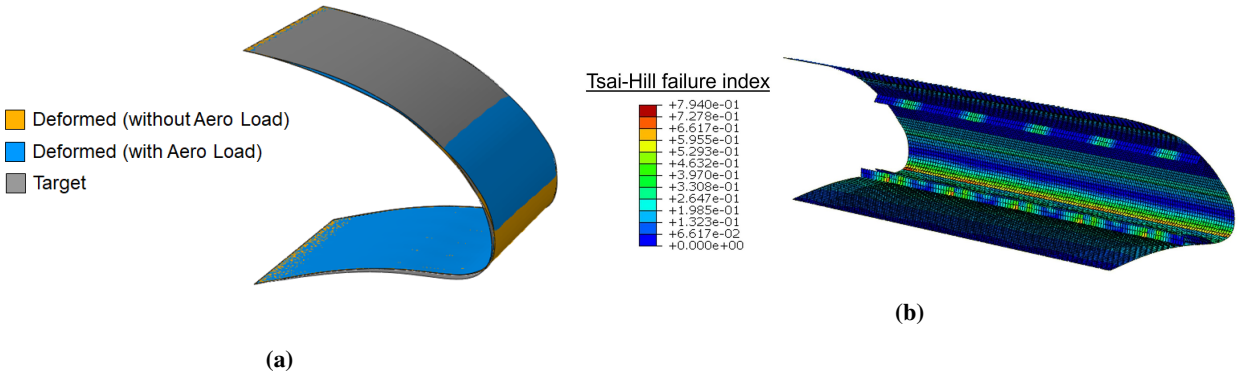

(a) **(b)**

Fig. 6 Numerical validation. Comparison between morphing deformed shapes and target shape (a). Tsai-Hill failure index in the skin (b).

In parallel with the verification phase, some modifications are introduced to the structural solution to find an engineering solution very easy to manufacture and to assemble. Regarding the lamination of the skin, it must be noted that the optimization variables related to the skin cause a discretization in constant-thickness sectors, resulting in some cases in an abrupt step between two adjacent thicknesses. This situation has been improved in the stacking phase by properly cutting the laminae to realize a gradual transition. It is expected that this solution will help in obtaining a more smooth deformation of the external surface. Skin, stringers, and spar are realized in glass-fibre fabric, with a curing process in dedicated molds. Another critical aspect of the manufacturing phase is related to the particular shape of the ribs. Milling is not practical, due to the various small holes and small-radius fillets. Instead, the water jet cutting technology is suitable for the manufacturing of the ribs geometry. The same technology is used for the cams and the rods of the kinematic chain. After the manufacturing phase, the complete prototype is assembled and set up for the laboratory tests, as shown in Fig. 7.

A. Experimental Setup and Testing

The main purpose of the experimental testing is to assess the functionality of the morphing droop nose. This is essential to validate the proposed morphing concept and to demonstrate the effectiveness of the engineering solution.

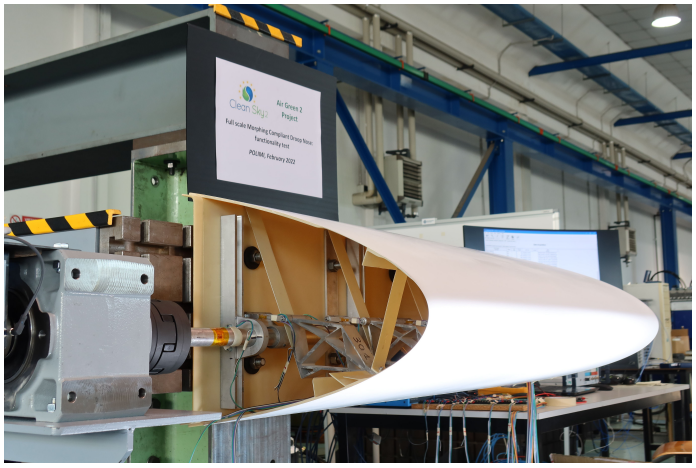

Fig. 7 Full–scale prototype for the functionality assessment.

In addition, the shape quality of the 3D morphing shape must be evaluated. The experimental shape achieved in the test can be identified by using an optical technology. In the first test campaign a full-field digital image correlation photogrammetry technique had been used, based on two high-resolution cameras and a dedicated software for the identification. A pattern made of black markers randomly distributed is painted on the surface for the digital image correlation. However, the use of only two cameras required to adopt a bottom view configuration and then a top view configuration, and to combine the two sets of results at the end of the test. In the following test, a different approach has been adopted. It is based on a motion capture system, provided by Qualisys. The system consists of eight 2MP cameras. The greater number of cameras enables to achieve an accurate reconstruction of the 3D motion of the entire external surface of the droop nose. Moreover, the capture rate of 100 Hz is high enough to catch the temporal evolution of the device, thus providing with the motion information at whatever intermediate deflection level from the undeformed configuration up to the maximum deployment of the device. Once the system is calibrated, the cameras track the position of spherical markers installed on the object of interest, and the software computes the trajectories of the markers. Starting from the displacement of the markers, a dedicated procedure has been developed to obtain, in the postprocessing phase, the identified positions of the entire surface of the droop nose. This procedure consists of an interpolation technique based on Radial Basis Functions (RBF), similar to the fluid-structure interpolation of displacements and loads typically used in aeroelasticity [15]. The coarser mesh where the displacements are known is represented by the markers distribution, thus the markers are the centers of the RBFs. The finer mesh describing the geometry where the displacements must be interpolated is represented by the numerical grid used in the finite element simulations. The number of markers and their location on the surface are chosen based on a greedy approach, which is aimed at finding a compromise between the number of markers and the expected local error from the interpolation. This approach is applied to the interpolation of the displacements of the numerical solution. A limited subset of nodes are used as markers, the remaining displacements are determined by interpolation, and this result is compared with the known finite element solution to obtain a quantification of the interpolation error. At the end, 155 markers are distributed on the surface, with a greater density of points in the leading-edge region, where the maximum curvature change occurs. Figure 8a depicts the arrangement of the cameras around the droop nose. Figure 8b shows the distribution of the spherical markers on the surface of the device. It must be noted that the pattern of black markers painted on the surface is not used in this test, whereas it was needed for the previously adopted photogrammetry technique.

The test setup also involves the installation of dedicated strain gauges to measure the torque on the shaft, the axial forces in the rods, and the bending strain in the skin. The installed sensors are shown in Fig. 9. The actuation torque is directly measured on the shaft, but it can be also estimated using the axial forces acting on the compliant ribs. Two sections are interested by the skin strain measure, located at 20% and 80% of the span respectively; the chordwise position of the sensor is located where the maximum curvature change is expected. Figure 10 represents the maximum principal strains in the skin computed by the FEM analysis. The locations of the described strain gauges on the skin are indicated by two black points. All these measures will be used to perform the numerical–experimental correlation. Based on the outcome of this correlation, the FEM model will be updated and used for further numerical analyses, reproducing the behavior of the experimental demonstrator.

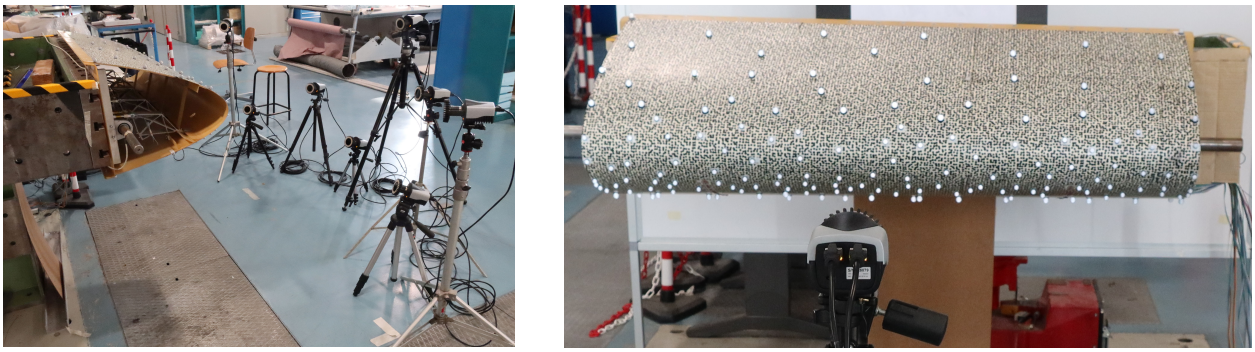

(a) (b)

Fig. 8 Setup for the motion capture system: position of the cameras (a) and markers distribution (b).

Fig. 9 Strain gauges installed on the full–scale prototype.

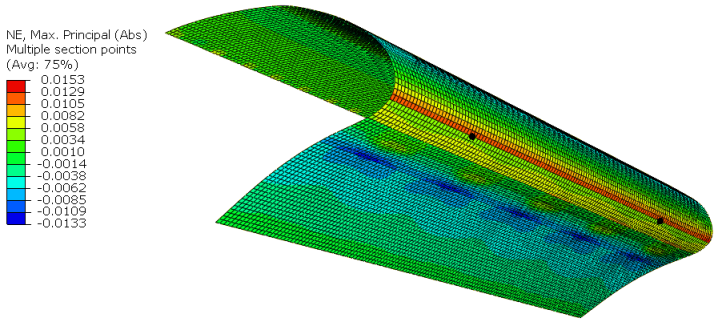

Fig. 10 Maximum principal strains in the skin. The black points represent the location of the strain gauges on the skin of the prototype.

The experimental testing is described in the following. The spar of the device, representing the spar of the wing–box, is constrained to the rig. A torque is applied to the shaft to realize the morphing deflection. The experimental test is performed up to a maximum shaft rotation of 65 deg. The strain sensors are continuously acquired during the deployment of the device, and the cameras track the motion of the markers. The equivalent rotation of the device is 12.5 deg. Figure 11 depicts the corresponding deformed shape.

Fig. 11 Deformed shape of the full–scale prototype at 65 deg of shaft rotation.

B. Shape identification

The motion capture software computes the position of the markers. Their initial position is used to compute matrix **H** of the interpolation, whose kernel is based on RBFs depending on the relative distance between the points. Then, the markers displacements with respect to the initial configuration are used to identify the displacements of the entire surface of the device, by means of the grid represented by the FEM mesh. Matrix **H** can be computed once for all, since it depends only on the initial geometry and the markers distribution. Then, the interpolation process can be applied to identify the experimental deformation for whatever deflection level reached in the test. In particular, the maximum deflection corresponding to 65 deg of shaft rotation is used to compare the experimental deformed shape with the numerical one. The comparison is very good as it will be shown in the next section, after the description of the numerical–experimental correlation, followed by the updating of the FEM model.

C. Numerical–Experimental Correlation

The experimental results, in terms of torque, strains, and shape are compared to the numerical ones to perform a numerical–experimental correlation. The experimental torque here reported is estimated from the axial forces in the rods, to filter the friction in the supports. Anyway, the friction computed as the difference between this estimation and the torque measured on the shaft is very small, thanks to the adoption of bearings. This represents an improvement with respect to the first test campaign.

The torque comparison between the numerical solution and the experimental result is represented in Fig. 12a. It shows that the experimental value is lower than the numerical FEM one. In particular, the numerical torque is 55% higher than the experimental one at 65 deg of shaft rotation. A similar discrepancy is found for the strain energy, which can be estimated by integrating the torque over the shaft rotation angle. The comparison between experimental strain energy and the numerical one is depicted in Fig. 12b. In this case, the numerical strain energy is 44% higher than the experimental one at 65 deg. The investigation of such discrepancy is conducted by evaluating the different contributions to the strain energy of the numerical model. It is found that the contribution of the skin represents the 91% of the strain energy of the whole model. Therefore, the updating of the FEM model can be performed acting on a skin-related quantity as updating variable, with the aim of minimizing the discrepancy between the numerical and the experimental results, in terms of strain energy. A suitable choice could be the thickness distribution of the skin that affects the strain energy with a dependence on the third power of the thickness. An alternative, which is adopted in this work, is the use of the elastic modulus of the glass-fibre fabric material as updating variable, assuming that the actual mechanical properties of the material can be lower than those reported in the data-sheet, as a result of the manufacturing process. Many factors could lead to this outcome, such as a different orientation of the fibres, or the difficulties related to overlapping the layers in the high-curvature mold. The simplest choice to realize the model updating is to introduce the same modification to the elastic modulus of all the skin sectors. Following this approach, a 31% reduction of the elastic modulus of the fabric allows to obtain an updated FEM model able to match the experimental strain energy, as shown in Fig. 12b. The actuation torque for the updated FEM model is reported in Fig. 12a. The comparison with the experimental torque has been improved, but the resulting match still exhibits some difference.

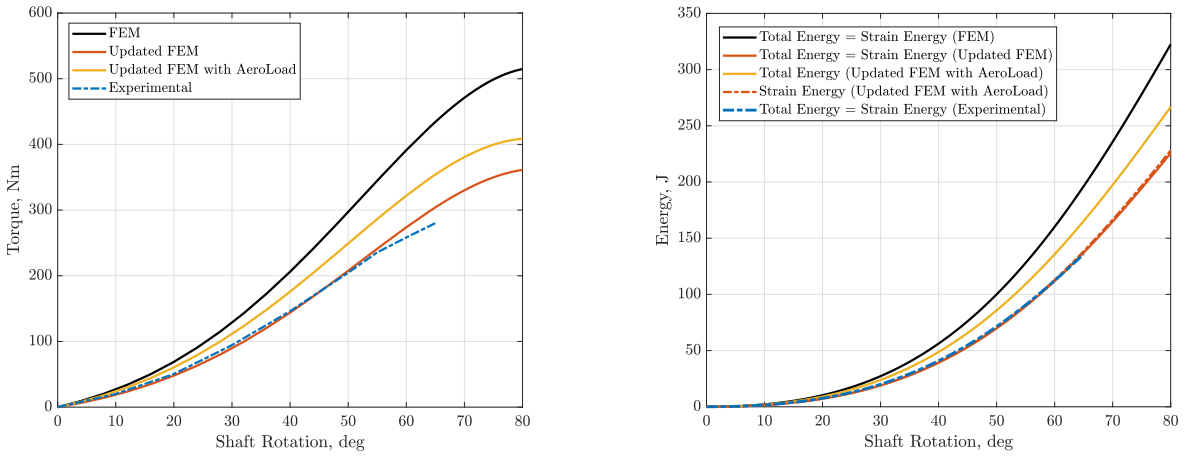

(a) **(b)**

Fig. 12 Numerical–experimental correlation: actuation torque (a) and energy (b) as functions of the shaft rotation.

The updating of the FEM model affects negligibly the morphing shape change computed by the numerical simulation. Figure 13a shows the comparison between the deformed shape of the updated FEM at 65 deg and the identified experimental shape obtained by motion capture and RBF interpolation. The difference between the two shapes is very small. A numerical quantification of the error can be done thanks to the availability of the deformed position of both shapes at corresponding points, which are the nodes of the FEM mesh. The local error is shown in Fig. 13b. It assumes greater values in the upper surface of the droop nose. The maximum local error is 7 mm, whereas the root mean square error computed over 14231 points is 4 mm.

The small difference between the deformed shapes is reflected also in the strain comparison reported in Fig. 14a, where the strains experimentally measured in the skin are 8% higher than the numerical ones.

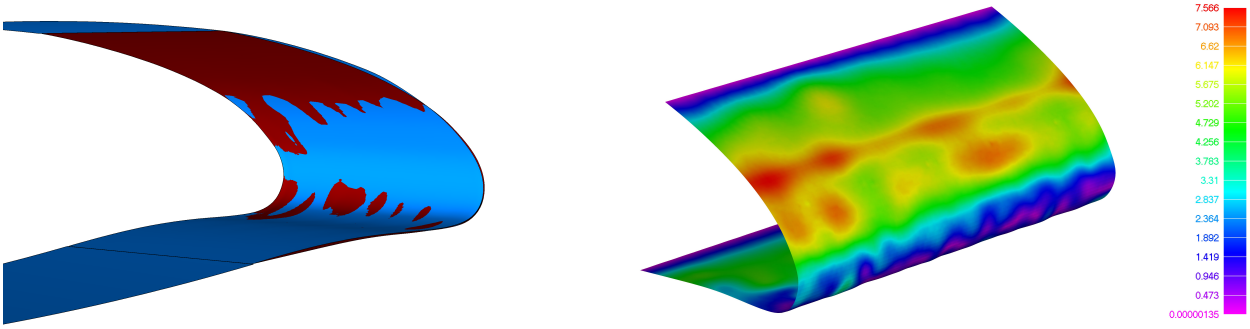

(a) **(b)**

Fig. 13 Comparison of the deformed shapes at 65 deg of shaft rotation. Identified experimental shape in dark red and FEM numerical shape in blue (a). Local error in mm between experimental and numerical shapes (b).

Once an updated FEM model is available, able to reproduce the behavior of the experimental prototype with a minimum error, it can be used to investigate other important aspects of the morphing device. For instance, the updated FEM model can be used to simulate the structural behavior of the device subjected to the aerodynamic loads coming from the fluid, in the aerodynamic conditions relevant for the use of the device. In particular, we are interested in evaluating how the application of the aerodynamic external loads affects the device in terms of deformation, shape change, performances, and energy. Thanks to the adopted multi-objective approach for the design of compliant structures, the deformation of the structure due to the application of loads should be limited. The verification is performed by

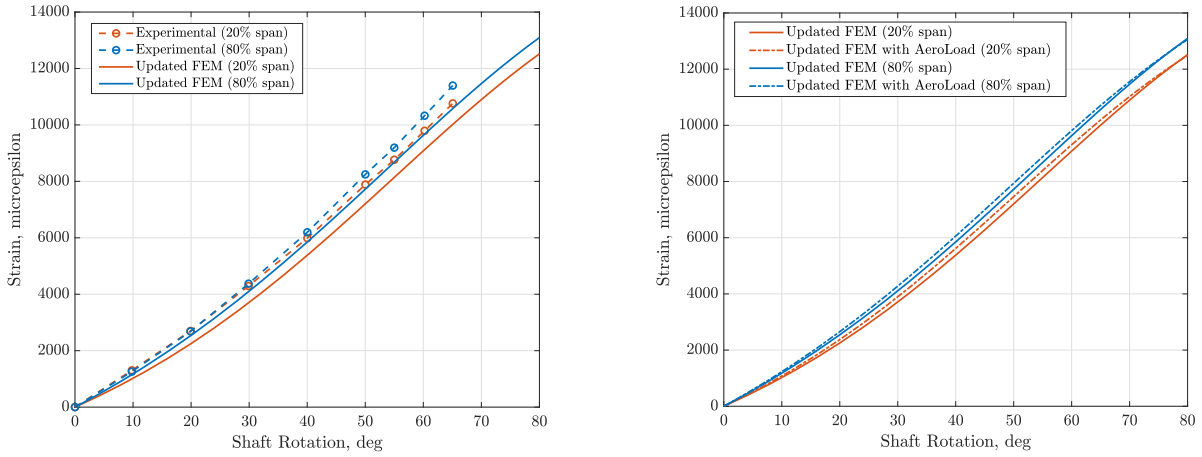

Fig. 14 Maximum strains in the skin as functions of the shaft rotation: comparison between numerical and experimental results (a) and comparison between numerical results with and without aerodynamic loads (b).

simulating the structural solution of the updated model under the pressure loads corresponding to the landing condition at an angle of attack of 10 deg. This solution is compared with the corresponding solution that was obtained without the external loads. The quantitative comparison between the numerical deformed shapes with and without external loads applied gives a root mean square error of 3 mm. Moreover, the increment in strains due to the external loads is very small, as shown in Fig. 14b. Therefore, at the local level, in terms of shape and strains the presence of the aerodynamic loads has a minimum effect. The situation is different from the energetic viewpoint. The total energy of the loaded device, which is reported in Fig. 12b, is the sum of two contributions. The former is the strain energy associated to the morphing shape change, the latter is the work associated to the external pressure loads. Figure 12b shows that the total energy of the loaded device is higher with respect to the energy of the device subject to actuation torque only. In particular, with equal shaft rotation and deflection level, the actuation energy required under loads is 18% higher with respect to the unloaded case. The corresponding actuation torque is 13% higher. Moreover, the contributions to the total energy can be divided as a 85% required to deform the structure and a 15% required to withstand the external loads. Therefore, for a leading-edge device the prevalent contribution to the required actuation energy is associated with the morphing process. Instead, the effect of the external aerodynamics loads is lower, though not negligible from the energetic viewpoint.

D. Aerodynamic Validation

The validation of the aerodynamic performances is done by means of Computational Fluid Dynamics (CFD) simulations performed with the open-source code SU2 [16]. The aim of the investigation is to compare the aerodynamic results of the correlated numerical model with those of the target shape.

The aerodynamic model is based on RANS equations, with Menter's Shear Stress Transport (SST) turbulence model, and a pseudotime CFL number of 20. The linear solver is a Flexible Generalised Minimum Residual (FGMRES).

The base geometry of the aerodynamic model corresponds to the aerodynamic surface located in the spanwise section of the droop nose prototype, as shown in Fig. 15. Two models are prepared, and they differ in the morphing leading-edge region only. The considered morphing shapes are:

- the deformed shape obtained from the correlated FEM model with a shaft rotation of 80 deg;
- the optimal target shape determined in the first step of the design procedure.

Regarding the mesh for the RANS simulation, the fluid domain is discretized using 6 millions nodes, with refining close to the airfoil surface, to correctly represent the turbulent boundary layer. The first cell is placed at a height of $y+ \approx 1$. The numerical model simulates a real experiment in the wind tunnel, where the wing is covering the entire span of the test section. Two walls, with no penetration boundary conditions, are placed at the root and tip of the wing. Far from the wing a Riemann farfield boundary condition is then imposed. The aerodynamic mesh is shown in Fig. 16.

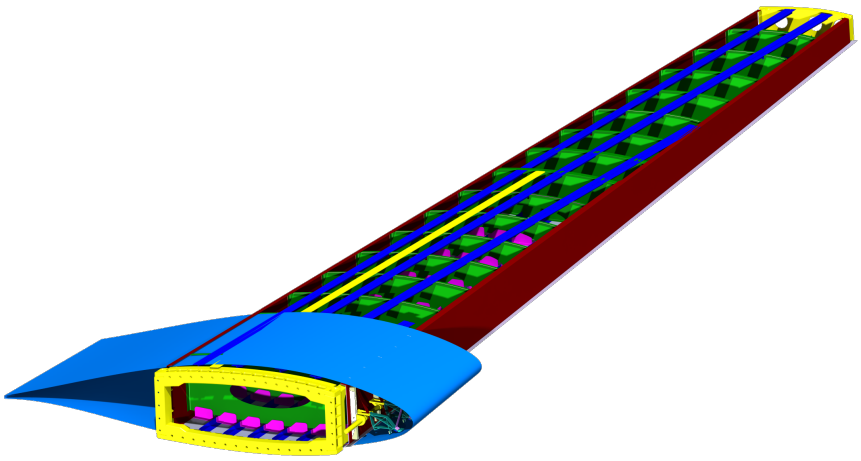

Fig. 15 Geometry of the aerodynamic demonstrator for the performance validation.

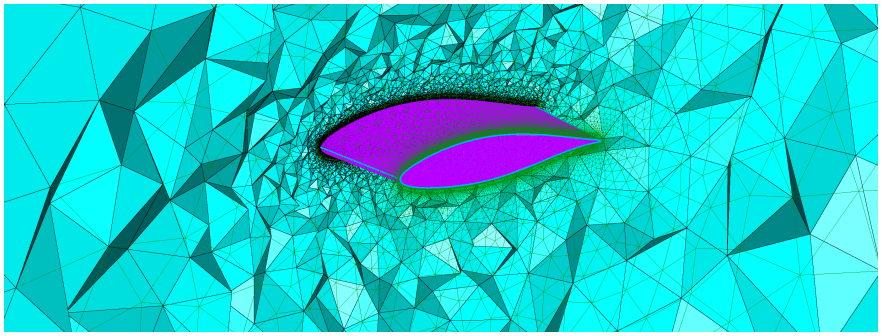

Fig. 16 Aerodynamic mesh for the CFD simulations.

The flight condition for the aerodynamic simulations is characterized by a Mach number Ma = 0.197, at sea level. Different angles of attack are considered, ranging from 0 deg to 18 deg. Figure 17a represents the lift coefficient as a function of the angle of attack, whereas Fig. 17b shows the polar curves. The comparison between the results of the deformed shape and the target ones shows negligible differences in terms of lift and drag coefficients.

The pressure coefficient distributions are compared at the stall angle $\alpha = 14°$, as shown in Fig. 18. While the polar comparison is globally satisfactory, the pressure distribution shows a discrepancy. This discrepancy can be attributed to an abrupt change of curvature of the deformed shape with respect to the target shape in that region. However, the comparison between numerical and experimental shape, as shown in Fig. 13, indicates that the considered region is characterized also by the maximum discrepancy between the shapes. Moreover, the experimental shape change is smoother than the numerical one, probably due to the gradual transition of the thickness between adjacent sectors. As a future work, the updating process of the FEM model could be improved using a different elastic module for each sector of the skin in order to obtain a better correlation of the shape. As a consequence, a better match of the aerodynamic performances should be achieved. Finally, an aeroelastic assessment, based on coupling CFD computations with nonlinear finite element analyses performed on the final updated FEM, will be carried out to validate the device and the aerodynamic performances also considering the aerodynamic field that changes during the deformation.

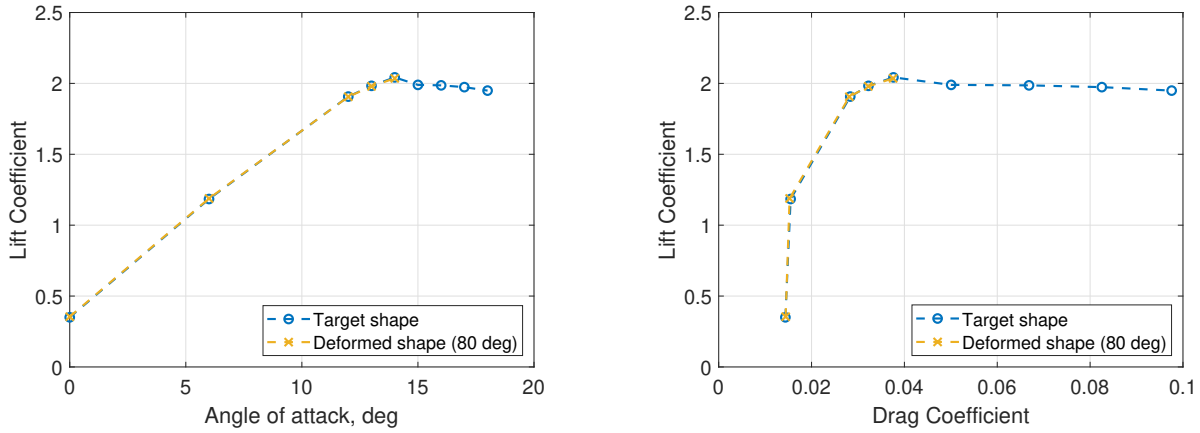

(a) **(b)**

Fig. 17 Comparison between CFD results of optimal target shape and FEM deformed shape: lift coefficient as a function of the angle of attack (a) and polar curves (b).

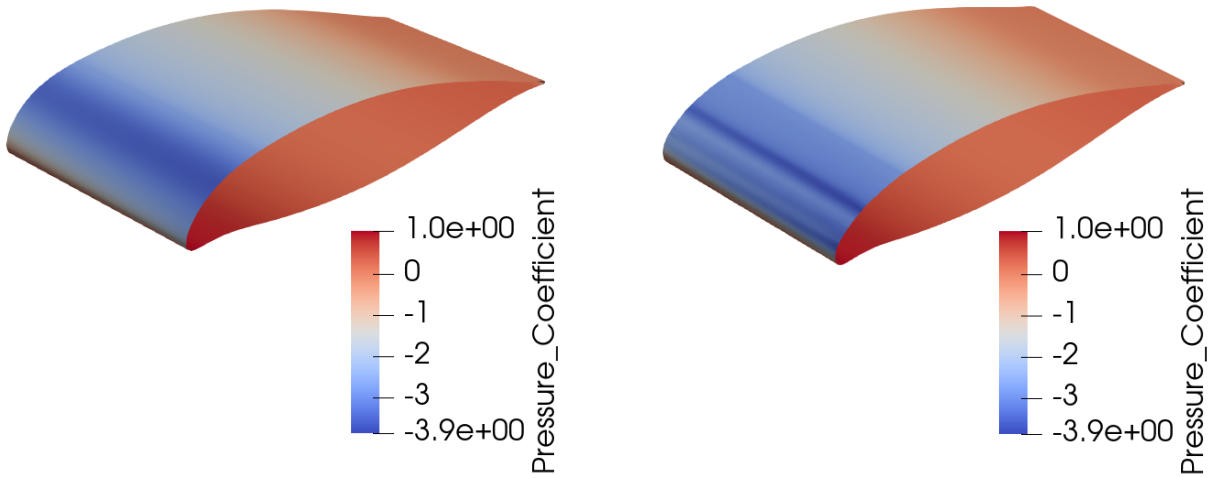

(a) **(b)**

Fig. 18 Pressure coefficients distribution: optimal target shape (a) and FEM deformed shape (b).

IV. Conclusion

This paper has described the validation of a morphing droop nose demonstrator in the framework of Clean Sky 2 REG-IADP AIRGREEN 2 (AG2) project. The device, designed to be installed on the innovative wing of a regional aircraft, has been conceived to provide high–lift capabilities in take–off and landing conditions, together with a smooth and gap–less skin surface. A multi–level and multi–disciplinary optimization procedure has been adopted for the design of the full–scale prototype made of actual aeronautical materials. The experimental tests performed on the prototype have assessed the functionality of the device and the quality of the deformed shape, demonstrating the effectiveness of the proposed morphing concept . A numerical–experimental correlation has been performed aimed at minimizing the discrepancy between experimental results and numerical simulations. Finally, the aerodynamic results of the deformed shape have been compared to the target ones to evaluate the actual performances of the morphing device.

Acknowledgments

The AirGreen2 Project has received funding from the Clean Sky 2 Joint Undertaking, under the European's Union Horizon 2020 research and innovation Programme, under grant agreement No. 807089.

References

[1] Gould, D. K., "Final Report, Variable Camber Wing Phase I," Tech. rep., D180-17606-1 (Contract No. N00014-73-C-0244), Research & Engineering Div., Boeing Aerospace Co, 1973.

[2] Decamp, R., and Hardy, R., "Mission adaptive wing advanced research concepts," *11th Atmospheric Flight Mechanics Conference*, 1984, p. 2088.

[3] Bonnema, K., and Smith, S., "AFTI/F-111 mission adaptive wing flight research program," *4th Flight Test Conference*, 1988, p. 2118.

[4] Smith, S. B., and Nelson, D. W., "Determination of the aerodynamic characteristics of the mission adaptive wing," *Journal of Aircraft*, Vol. 27, No. 11, 1990, pp. 950–958.

[5] Kota, S., Osborn, R., Ervin, G., Maric, D., Flick, P., and Paul, D., "Mission adaptive compliant wing–design, fabrication and flight test," *RTO Applied Vehicle Technology Panel (AVT) Symposium*, 2009.

[6] Woods, B. K., Bilgen, O., and Friswell, M. I., "Wind tunnel testing of the fish bone active camber morphing concept," *Journal of Intelligent Material Systems and Structures*, Vol. 25, No. 7, 2014, pp. 772–785. https://doi.org/10.1177/1045389X14521700.

[7] Vasista, S., Riemenschneider, J., van de Kamp, B., Monner, H. P., Cheung, R. C., Wales, C., and Cooper, J. E., "Evaluation of a compliant droop-nose morphing wing tip via experimental tests," *Journal of Aircraft*, Vol. 54, No. 2, 2016, pp. 519–534. https://doi.org/10.2514/1.C033909.

[8] Kintscher, M., Wiedemann, M., Monner, H. P., Heintze, O., and Kühn, T., "Design of a smart leading edge device for low speed wind tunnel tests in the European project SADE," *International Journal of Structural Integrity*, Vol. 2, No. 4, 2011, pp. 383–405.

[9] Sodja, J., Martinez, M. J., Simpson, J. C., and De Breuker, R., "Experimental evaluation of a morphing leading edge concept," *Journal of Intelligent Material Systems and Structures*, Vol. 30, No. 18–19, 2019, pp. 2953–2969. https://doi.org/10.1177/1045389X19862369.

[10] Vasista, S., Tong, L., and Wong, K. C., "Realization of Morphing Wings: A Multidisciplinary Challenge," *Journal of Aircraft*, Vol. 49, No. 1, 2012, pp. 11 – 28. https://doi.org/10.2514/1.C031060.

[11] Cavalieri, V., De Gaspari, A., and Ricci, S., "Optimization of compliant adaptive structures in the design of a morphing droop nose," *Smart Materials and Structures*, Vol. 29, No. 7, 2020, p. 22. https://doi.org/10.1088/1361-665X/ab8902.

[12] De Gaspari, A., "Multiobjective Optimization for the Aero-Structural Design of Adaptive Compliant Wing Devices," *Applied Sciences*, Vol. 10, No. 18, 2020, p. 30. https://doi.org/10.3390/app10186380.

[13] Kulfan, B. M., "Universal Parametric Geometry Representation Method," *Journal of Aircraft*, Vol. 45, No. 1, 2008. https://doi.org/10.2514/1.29958.

[14] De Gaspari, A., and Moens, F., "Aerodynamic Shape Design and Validation of an Advanced High-Lift Device for a Regional Aircraft with Morphing Droop Nose," *International Journal of Aerospace Engineering*, Vol. 2019, 7982168, 2019, pp. 1 – 22. https://doi.org/10.1155/2019/7982168.

[15] Beckert, A., and Wendland, H., "Multivariate interpolation for fluid-structure-interaction problems using radial basis functions," *Aerospace Science and Technology*, Vol. 5, No. 2, 2001, pp. 125–134. https://doi.org/10.1016/S1270-9638(00)01087-7, publisher: Elsevier.

[16] Palacios, F., Alonso, J., Duraisamy, K., Colonno, M., Hicken, J., Aranake, A., Campos, A., Copeland, S., Economon, T., Lonkar, A., Lukaczyk, T., and Taylor, T., "Stanford University Unstructured (SU^2): An open-source integrated computational environment for multi-physics simulation and design," *51st AIAA Aerospace Sciences Meeting including the New Horizons Forum and Aerospace Exposition*, American Institute of Aeronautics and Astronautics, Grapevine (Dallas/Ft. Worth Region), Texas, 2013, p. 60. https://doi.org/10.2514/6.2013-287.